ACS APPLIED POLYMER MATERIALS

pubs.acs.org/acsapm

Article

Effect of Monomers and Deposition Conditions on Capacitive Polymer Films Prepared Using Oxidative Multilayers

Lauri Marttila,* Mikko Salomäki,* Henri Kivelä, Jukka Hassinen, Sari Granroth, Ermei Mäkilä, Johan Nyman, and Jukka Lukkari*

Cite This: https://doi.org/10.1021/acsapm.2c01366

Read Online

ACCESS | Metrics & More | Article Recommendations | Supporting Information

ABSTRACT: Oxidative layer-by-layer multilayers, consisting of polyphosphate (PP), Ce(IV), and graphene oxide, are a general platform for the electrodeless, spatially resolved deposition of redox-active and capacitive films of conducting polymers and melanin-type materials. However, the film formation process has not been closely examined. We show that PP plays a crucial role in the structure, stability, and function of the multilayers. Random P−O−P bond cleavage in PP at low pH rapidly decreases the effective chain length and, together with the lower complexing capacity of the Ce(III) species, leads to the dissolution of the oxidative multilayer during the polymer film deposition. The multilayer dissolution takes place during, e.g., poly(3,4-ethylenedioxythiophene) (PEDOT) film formation, and produces a homogeneous polymer film on the substrate. On the other hand, polymerization of 5,6-dihydroxyindole (DHI), an analogue of polydopamine, is carried out at higher pH, and the DHI-melanin film forms only on the outer surface, leaving the bulk of the multilayer intact. This leads to a poor electrical contact between the substrate electrode and the redox-active polymer film. Low pH and long deposition times are, therefore, beneficial for the formation of good-quality redox-active polymer films. PEDOT films prepared using oxidative multilayers have good specific volume and mass capacitance, and good retention of their capacitance. Capacitance spectroscopy revealed the contribution of different dynamic processes and showed that the redox processes limit their capacitance in the 100 ms timescale, restricting the power density of the film. The capacitance of the DHI-melanin films decreases drastically in the same timescale while the capacitance and charge storage capacity values remain higher than those of the PEDOT films. Improving the electrical connection to the substrate using alternative deposition techniques and increasing the film conductivity will make the DHI-melanin films promising components for biodegradable supercapacitors.

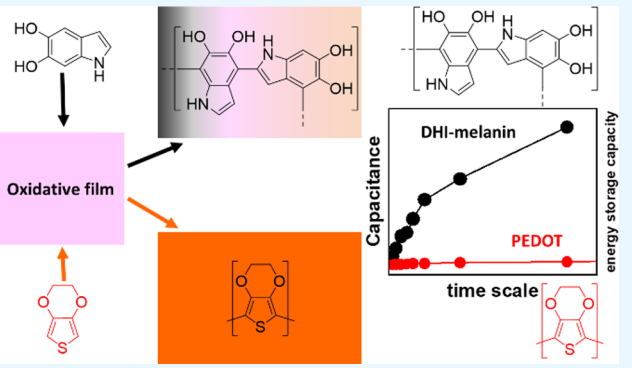

KEYWORDS: *layer-by-layer, PEDOT, melanin, supercapacitor, polyphosphate*

INTRODUCTION

The layer-by-layer (LbL) sequential assembly of polyelectrolytes has been shown to be a very general technique for a controlled and reproducible preparation of thin films.[1] It is insensitive to the nature, size, or form of the substrate and allows us to create thin films with an almost unlimited variation in composition and structure without sophisticated experimental set-up or strictly controlled ambient conditions. In its simplest form, it can be realized by dipping the surface alternately in dilute aqueous solutions of a polyanion and polycation (dip-LbL). This method is, however, time-consuming and material-inefficient, whereas the spin-and-spray LbL method offers greatly accelerated growth, and improved film morphology and material efficiency.[2]

We have recently demonstrated that LbL multilayers prepared using inorganic polyphosphate (PP), Ce(IV) ions, and graphene oxide (GO) are oxidative multilayers that can be used as general platforms for electrodeless preparation of capacitive films.[2−6] Such capacitive films can be used in supercapacitors for energy storage purposes. Supercapacitors have many beneficial properties such as a high power density, long cycle life, and high operating safety. Simple electrochemical double-layer capacitors (EDLCs) store energy electrostatically within the electrical double layer at the electrode−solution interface and their electrodes are often made from conductive and high-surface-area carbon materials.[7] However, the downside of such supercapacitors is that they have much lower energy density compared to, e.g., batteries, and in pseudocapacitors, some of their power density and cycle

Received: August 5, 2022
Accepted: December 5, 2022

life are sacrificed to enhance it.[7] These capacitors store energy in the oxidation state of the electroactive materials, and their electrodes are often made using conducting polymers or metal oxides.

Transient electrical devices could be used in many applications such as environmental monitoring, consumer electronics, data-secure hardware, and implantable medical devices.[8] These target applications set high requirements for the energy storage materials powering the devices. They need to be nontoxic, biocompatible, biodegradable, and still have satisfactory mechanical and electrochemical properties.[9] The conducting polymer poly(3,4-ethylenedioxythiophene) (PEDOT), for example, has good biocompatibility,[10,11] and it can be used in the supercapacitors powering implantable bioelectronics.[12] Conducting polymers, however, are not generally biodegradable.[10] One of the attractive material candidates for biocompatible and biodegradable supercapacitors is eumelanin, a ubiquitous quinone-based pigment in nature.[13−15] Eumelanin is a disordered and amorphous material with complicated structure[16] consisting of 5,6-dihydroxyindole (DHI) and 5,6-dihydroxyindole-2-carboxylic acid (DHICA) as its basic monomeric constituents in various redox states and tautomeric forms. In addition to the redox activity, eumelanin has a broadband UV−vis absorbance, and it can effectively bind many metals.

A synthetic eumelanin analogue DHI-melanin can be produced simply by oxidizing 5,6-dihydroxyindole.[17−20] Similar to polydopamine coatings,[21] the immersion of a substrate in a dilute neutral solution of DHI leads to the formation of thin DHI-melanin coating on its surface.[20] However, due to the simultaneous aggregation of DHI in the solution phase, the self-limiting thickness in a single-deposition step is limited to ca. 20 nm.[20] More advanced DHI-melanin film fabrication methods include matrix-assisted pulsed laser evaporation,[22] electrochemical polymerization,[23,24] and ammonia-induced solid-state polymerization.[14,25] We have previously shown that oxidative multilayer films with a general structure $(PP/Ce/GO/Ce)_n$ are suitable for the generation of bioinspired electroactive melanin-type films from 5,6-dihydroxyindole (DHI).[2,5] In these multilayers, the role of the graphene oxide in the film is to enhance the multilayer growth and its mechanical properties, whereas Ce(IV) acts as an oxidant.[6] Our aim has been to use oxidative multilayer films as a general method for the preparation of thin films for biocompatible and/or biodegradable supercapacitors. The specific volumetric capacitance obtained for thin $(PP/Ce/(r)GO/Ce)_n$/PEDOT films is in the range of 120−140 F cm^{-3} (60−70 F g^{-1}), and the $(PP/Ce/rGO/Ce)_n$/(DHI-melanin) films have considerably higher areal capacitance than the PEDOT-based films.[2] These results were encouraging for the further optimization of oxidative multilayer films for the preparation of electroactive films on desired substrates.

Despite the success of oxidative films as platforms for polymer film formation their precise structure and action are unknown. In this work, we have undertaken a more detailed depth profiling of the oxidative multilayers covered with PEDOT or DHI-melanin films using, e.g., the recently introduced argon gas cluster ion sputtering to minimize the chemical changes in the films.[26,27] We also evaluated their charge transfer kinetics and electrochemical stability using electrochemical impedance spectroscopy and cyclic voltammetry, and showed how the polymer film formation conditions affect the underlying oxidative multilayer.

Finally, we have now also detailed the role of polyphosphate (PP) in the oxidative multilayers. We have previously characterized other components of the oxidative multilayers quite thoroughly.[3,6] Polyphosphate is a polymer of orthophosphoric acid consisting of tetrahedral PO_4 units joined together via P−O−P bonds. Inorganic polyphosphates are large nontoxic and biodegradable polyanions, which effectively complex many cations. They can be branched polymers, which are rapidly hydrolyzed in aqueous media, or linear polymers found in the cells of all living organisms, which makes them an important completely inorganic biomolecule; they were long considered a molecular fossil but are now known to participate in many vital biological functions.[28−32] We show that they play also an important role in the structure and function of the oxidative multilayers.

EXPERIMENTAL SECTION

Materials. Ammonium cerium(IV) nitrate (Sigma-Aldrich), potassium ferricyanide (J.T. Baker), potassium ferrocyanide trihydrate (Merck), sodium dihydrogen phosphate monohydrate (J.T. Baker), sodium sulfate (VWR), sodium chloride (J.T. Baker), sodium hydroxide (Sigma-Aldrich), natural graphite flakes (mesh 325, 99.8%; Alfa Aesar), sodium nitrate (Riedel), potassium permanganate (Oy Tamro Ab), 5,6-diacetoxyindole (TCI), 3,4-ethylenedioxythiophene (EDOT, TCI), *N*-trimethoxysilylpropyl-*N*,*N*,*N*-trimethylammonium chloride (TMSPA, 50% in methanol, ABCR), sulfuric acid (>95%, Fisher Scientific), glacial acetic acid (VWR), hydrogen peroxide (30%, VWR), ammonium hydroxide solution (c.a. 25%, Sigma-Aldrich), methanol (Riedel-de Haën), and ethanol (Etax AaS, ALTIA, Finland) were used as received. Potassium metaphosphate (98%, ABCR) was washed on a Büchner funnel with water and dried at 110 °C to remove residual phosphoric acid. Graphene oxide was prepared from graphite using the modified Hummers method (see the Supporting Information (SI) for details). The graphene oxide dialysis was performed using a 3500 molecular weight cutoff membrane (Thermo Scientific SnakeSkin). All aqueous solutions were prepared in water distilled twice in quartz vessels. Materials in the study of polyphosphate degradation are described separately in the Supporting Information.

Substrates. The films were assembled on glass slides with indium tin oxide (ITO) coating on one surface. The substrates were washed in a 5:1:1 (v/v/v) solution of H_2O, 25% ammonium hydroxide, and 30% H_2O_2 for 30 min, rinsed with water, and dried first with N_2 gas and then at 110 °C. Dry substrates were pre-treated with 1:9 v/v TMSPA/methanol solution for 10 min, washed with methanol and water, and dried with N_2 gas to obtain positively charged surfaces.

Layer-by-Layer Film Fabrication. The oxidative $(PP/Ce/GO/Ce)_n$ multilayer films were prepared from 10 mM ammonium cerium(IV) nitrate, polyphosphate, and graphene oxide. Polyphosphate solution (10 mM) was prepared by mixing 10 mM KO_3P and 0.1 M NaCl and stirring overnight; a fresh solution was always used to minimize polyphosphate hydrolysis. GO was exfoliated in an ultrasonication bath (VWR USC500THD) for 30 min to prepare a 0.3 mg/ml GO suspension, and was used without delay. The oxidative multilayer films were fabricated using an automated house-made spin-spray multilayer deposition device.[2] The precursor solutions were sequentially sprayed on a horizontally spinning substrate (1500 ± 200 rpm) using the spraying scheme previously described.[2] All films were rinsed with water and dried with nitrogen flow.

Polymerization of PEDOT and DHI-Melanin. EDOT and DHI were oxidized on an oxidative $(PP/Ce/GO/Ce)_n$ multilayer films for 17 h at pH 1.5 and for 2 h at pH 4.5 respectively (see the Supporting Information for details).

Film Characterization. *Electrochemistry.* Electrochemical measurements were made in a three-electrode configuration and all solutions were deaerated with N_2. A platinum wire was used as an auxiliary electrode and a Ag/AgCl (eDAQ, ET072) as a reference electrode. All potentials are referred to this reference, and its potential

https://doi.org/10.1021/acsapm.2c01366
ACS Appl. Polym. Mater. XXXX, XXX, XXX−XXX

was checked against a Ag/AgCl (sat. KCl) laboratory standard before and after every measurement series (deviation less than ±2 mV). Measurements were done using either an IviumStat potentiostat (Ivium Technologies) or a PalmSens4 potentiostat (PalmSens). The impedance spectra fitting was made with Palmsens PSTrace 5.8 software. Additional details are given in the Supporting Information. The effect of the electrochemical reduction of GO was studied by X-ray photoelectron spectra (XPS) at several locations on a dry (PP/Ce/(r)GO/Ce)$_{15}$/(DHI-melanin) film, and the film thickness and surface roughness were estimated with scanning white light interferometry and atomic force microscopy (AFM), respectively.

X-ray Photoelectron Spectroscopy (XPS). X-ray photoelectron spectra were measured with a Thermo Scientific Nexsa X-ray photoelectron spectrometer using monochromated Al Kα (1486.6 eV) X-ray radiation. Reflection electron energy loss spectra (REELS) were measured with the same device. For depth profiling and high-resolution XPS analysis of contamination-free surfaces, the films were gently etched with MAGCIS dual mode ion source using an argon gas cluster ion beam with 4 eV cluster energy per atom (unless otherwise specified). All XPS spectra were analyzed with Thermo Scientific Avantage software (v5.9925) using a Shirley background and mixed Gaussian/Lorentzian product function with an L/G mix value of 30% in the peak fitting.

Scanning White Light Interferometry (SWLI). For thickness analysis, the DHI-melanin-based film was etched with monatomic Ar^+ beam after Ar cluster depth profiling until a clear indium signal was observed in the XPS survey spectrum. The thickness of the film was estimated with a custom-made scanning white light interferometer as the average mean step height from 6 data points. A detailed description of the instrument is provided in the Supporting Information.

SEM-EDS and AFM. The scanning electron microscopy (SEM) images were taken with Thermo Scientific Apreo S field-emission SEM. Secondary electron micrographs were obtained from uncoated samples at a pressure of 100 Pa (H_2O) using a low-vacuum detector. EDS spectra were collected and analyzed using an Oxford Instruments Ultim Max 100 detector with AZtec v4.1 software. Atomic force microscope (AFM) images were measured with Park Systems Park NX10 in a noncontact mode. The AFM images were processed and analyzed using Gwyddion 2.60 software. RMS surface roughness of the films was estimated after excluding grains by 50 nm threshold criteria.

NMR Spectroscopy. The ^{31}P NMR spectra were acquired with a Bruker Avance 400 FT NMR spectrometer (^{31}P: 161.8 MHz) equipped with a 5 mm BBO (broadband observe) probe using (nondeuterated) H_2O as solvent at 25.0 °C, without field-frequency lock. The temperature was calibrated with an ethylene glycol standard sample (80% ethylene glycol in DMSO-d_6, Bruker Biospin). The ^{31}P NMR spectra were measured with the standard Bruker pulse-acquire sequence *zg* using a 6.9 μs 90° excitation pulse (*p*1), 0.56 s acquisition time (aq), 1.0 s relaxation delay (*d*1), 14.6 kHz spectral width (swh), and 500−1000 scans (ns). (For the analysis of the ^{31}P NMR spectra and estimation of the shielding constants, see the SI.)

RESULTS AND DISCUSSION

Degradation of Polyphosphate. Polyphosphates are rather stable at physiological pH but are hydrolytically degraded in aqueous solutions due to the cleavage of the P−O−P bonds by water. The degradation rate is known to depend on pH, temperature, counterion, and polyphosphate concentration.[32] In general, low pH and high temperature increase the degradation rate, while metal cations may either enhance or inhibit the degradation, and different degradation reactions have been suggested for linear polyphosphate chains. Monomeric orthophosphate units can be cleaved from the chain ends in a reaction, long chains can be cleaved in the middle to generate shorter segments, and a nonhydrolytic formation of cyclic trimetaphosphate anions has been suggested. The mechanism of the hydrolytic cleavage involves a nucleophilic attack of a water molecule to a positively charged phosphorus atom,[33] and at lower pH, protonation of the P═O moiety leads to acid catalysis.

In the oxidative multilayers, the PP chains effectively bind other components together by coordinatively bonding to the metal ions.[6] In addition, they modify the mechanical properties of the multilayers. Therefore, the stability of the PP chains is important for the applications of oxidative multilayers. The degradation reactions have been studied using titrimetric, chromatographic, and viscometric methods, and especially, by nuclear magnetic resonance spectroscopy.[34] Especially, ^{31}P NMR is the most straightforward method to study polyphosphate chain degradation. All of the studies of PP degradation are rather old, and we have considered it necessary to have a closer look at the behavior of PP in different conditions using ^{31}P NMR spectroscopy. In linear polyphosphates, the phosphorus signals can be divided into three main groups. The final degradation product, orthophosphate (O), is usually taken as the reference signal (0 ppm). The chemical shift of the phosphorus atoms in the middle of the chain (M) is ca. −20 ppm, and that of the atoms at the chain ends (E) ca. −10 ppm.[34] In the spectrum of a highly degraded PP sample the M (and E) signals show several overlapping multiplets (Figure S2) because in short chains the chemical shifts of the different phosphorus atoms can be differentiated. However, we could not observe signals attributable to branching sites (chemical shift estimated at ca. −50 ppm), which suggests that the PP used is a linear polymer.

The signals due to the end groups allow the estimation of the number average molar mass of the polymer (Figure 1, see the SI for details). Because of the noise in the spectrum, the longest chain lengths that could be reliably determined were ca. 1600 monomer units. At pH 2, the end group signal was detected already after a couple of hours, but at pH 4, only after ca. 60 h (Figure S2). When PP was dissolved in pure water (with 100 mM NaCl, initial pH ca. 4.5) the end group signal appeared after ca. 7 days and no orthophosphate signal was observed even after more than 40 days. This shows that the cleavage of the PP chains preferably takes place in the middle of the chain and not at the ends. We can obtain a simple kinetic model for PP degradation by considering the cleavage of individual bonds. During the hydrolysis, the total number of

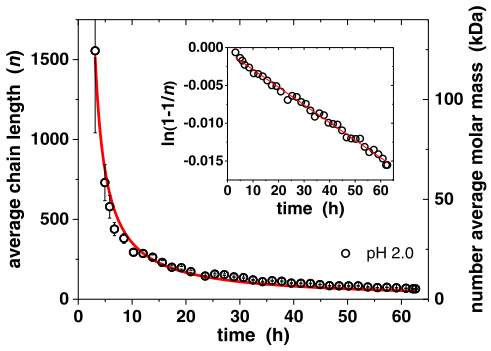

Figure 1. Degradation of inorganic polyphosphate at pH 2 (298 K; 40 mM potassium polyphosphate in 100 mM NaCl + 10 mM phosphoric acid; for the calculation of the error bars, see the SI). The line is a fit to the kinetic degradation model discussed in the text. The cations are not included in the number average molar mass. The inset shows the linearization of the model.

https://doi.org/10.1021/acsapm.2c01366
ACS Appl. Polym. Mater. XXXX, XXX, XXX−XXX

monomer units remains constant (includes also possible monophosphates) and the number of chains (monomers included) increases by one per every bond cleavage, independent of its location (either in-chain or terminal). If we assume that the probability of the P−O−P bond cleavage does not depend on the position of the bond in the chain or the chain length (assumed valid down to relatively short chains) we obtain a kinetic equation for the average chain length in the PP sample as (see the SI)

$$n = \left[1 - \frac{B_0}{P_0}\exp(-t/\tau)\right]^{-1}$$

Here B_0 and P_0 are the initial number of P−O−P bonds and monomer units in the sample, respectively, and τ is the time constant for the bond cleavage. Figure 1 shows a fit of the model to the NMR data for the PP degradation at pH 2, and also the linearization of the model (inset). The model well describes the process, yielding $B_0/P_0 = 1.0$, as expected for long polymer chains, and $\tau = (3160 \pm 40)$ h for the P−O−P bond cleavage time constant (error refers to the standard deviation of the fit parameter; note that the nonlinear model weighs the most important first data points more than the linearized form, see the SI for discussion). The success of the model supports the hydrolysis mechanism involving the P−O−P cleavages mainly in the bulk of the chain; we were not able to detect any cyclic products. In spite of the long time constant, the average chain length decreases rapidly during the first 10 h because the hydrolysis effectively splits longer chains. This has important consequences for the oxidative multilayers because the deposition of PEDOT takes place at low pH.

Film Composition. The $(PP/Ce/GO/Ce)_{15}$, $(PP/Ce/GO/Ce)_{15}$/PEDOT, and $(PP/Ce/GO/Ce)_{15}$/(DHI-melanin) films were analyzed with X-ray photoelectron spectroscopy (XPS) to obtain information about the film composition before and after the polymer film formation onto the oxidative multilayer. The attenuation length of the XPS photoelectrons in the oxidative multilayer is ca. 3 nm, and thus the technique provides information about the outermost part of the sample surface.[5] Therefore, the composition and chemical structure of the film interior were studied by sputtering them using low-energy argon clusters. This minimizes the chemical changes of polymeric materials during sputtering and produces a more reliable depth profile.[26,27]

Film Composition. $(PP/Ce/GO/Ce)_{15}$/PEDOT. EDOT was polymerized onto a $(PP/Ce/GO/Ce)_{15}$ film from an aqueous monomer solution at pH 1.5 (H_2SO_4). The composition of the oxidative film is discussed in the Supporting Information. The SEM image (Figure S6) shows that the $(PP/Ce/GO/Ce)_{15}$/PEDOT film surface is smooth and uniform, except that structures due to GO are still visible. The survey spectrum is dominated by the C 1s, O 1s, and S 2p peaks, and the Ce and P signals are greatly attenuated (Figure S6). The depth profiling, which was continued until the indium signal was observed, shows that the atomic composition of the $(PP/Ce/GO/Ce)_{15}$/PEDOT film is very uniform throughout the film, including the outermost surface (Figure 2). Cerium and phosphorus are almost completely depleted from the whole film, indicating that the film is practically pure PEDOT with some remaining GO after the polymerization step. High-resolution XPS spectra of the $(PP/Ce/GO/Ce)_{15}$/PEDOT film are well in accordance with that of a PEDOT polymer, further evidencing that PEDOT produced via oxidative

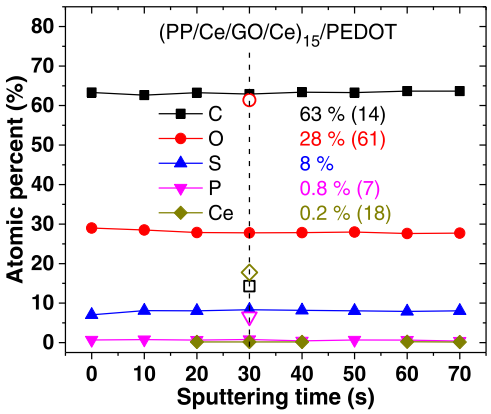

Figure 2. Relative atomic concentrations of $(PP/Ce/GO/Ce)_{15}$/PEDOT film during depth profiling. The relative atomic concentrations of the sputtered $(PP/Ce/GO/Ce)_{15}$ film are shown for comparison (open symbols and percentages in parentheses).

multilayers is similar to PEDOT produced by other techniques (see the Supporting Information for details). The uniform composition of the film and lack of PP and Ce can be attributed to the rapid hydrolysis of polyphosphate under the highly acidic conditions applied during EDOT polymerization. The hydrolysis breaks the coordinative Ce-PP network and leads to the dissolution of the phosphates in the polymerization solution. The low complexing power of the Ce(III)-ion also prevents its complexation by the coordinative groups in the remaining GO.[5] The dissolution of the multilayer framework provides also a natural explanation for the previously observed shrinkage of the film after PEDOT formation.[2] The C:O:S atomic ratio of the $(PP/Ce/GO/Ce)_{15}$/PEDOT film is 7.6:3.3:1 (an average of 19 measurements from the argon cluster sputtered film with 2−8 eV energy per Ar^+ atom), close to 6:2:1 expected for pure PEDOT. The higher amounts of carbon and oxygen can be attributed to the remaining GO in the film implying that PEDOT amounts to ca. 80% of the mass of the film.

Film Composition. $(PP/Ce/GO/Ce)_{15}$/(DHI-melanin). DHI-melanin was oxidized onto the $(PP/Ce/GO/Ce)_{15}$ film at pH 4.5. The resulting film has a globular surface structure (Figure S9), similar to that of a eumelanin/(graphene-type) hybrid material.[35] The high ridges seen in Figure S9a correspond in size to the GO flakes, and they disappear after the reduction of GO, which can be attributed to the wrapping of the GO sheets upon reduction.[36] Excluding the ridges, the RMS surface roughness of the film is low, ca. 19 nm (from 10 × 10 μm^2 images), unaffected by the electrochemical reduction of GO, and close to the values of the corresponding $(PP/Ce/GO/Ce)_{15}$ and $(PP/Ce/GO/Ce)_{15}$/PEDOT films.[2] The thickness of the $(PP/Ce/rGO/Ce)_{15}$/(DHI-melanin) film is ca. 270 nm, as estimated by scanning white light interferometry (Figure S14). Unfortunately, the method could not be used for the $(PP/Ce/GO/Ce)_{15}$/(DHI-melanin) film because the contrast was too low in this case.

The molecular structure of the DHI-melanin is complicated but it is thought to be composed of indole-based oligomers (dihydroxyindole, DHI, its oxidized form indolequinone IQ, and its tautomeric forms quinone methide QM, and quinone imine QI; Figure 3a) and their oxidative ring-cleavage products, such as pyrrolecarboxylic acid moieties.[17−19,37] Theoretical calculations show that DHI is the most stable

https://doi.org/10.1021/acsapm.2c01366
ACS Appl. Polym. Mater. XXXX, XXX, XXX−XXX

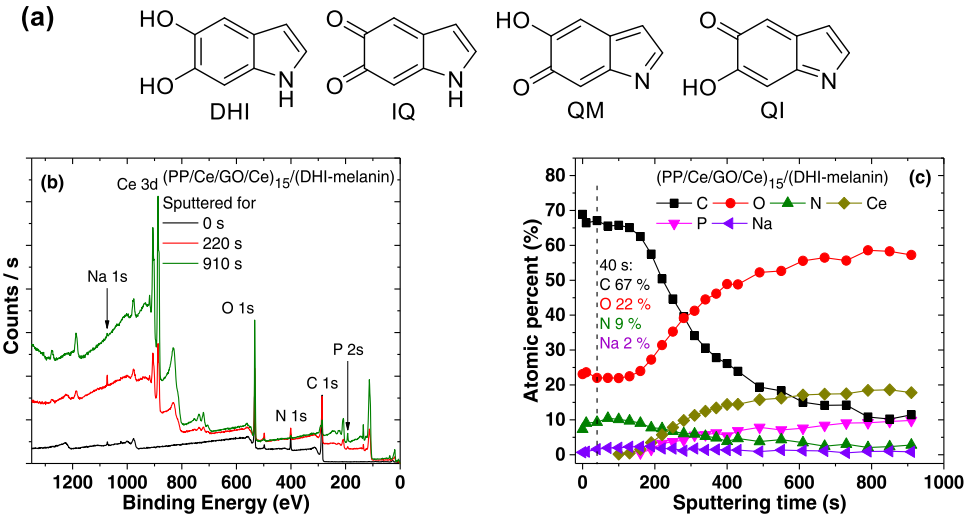

Figure 3. (a) Structures of 5,6-dihydroxyindole (DHI), and different tautomers of its oxidized form (5,6-indolequinone, IQ; quinone methide, QM; quinone imine, QI). (b) Survey spectrum of the $(PP/Ce/GO/Ce)_{15}$/(DHI-melanin) film at different sputtering stages. (c) Relative atomic concentrations of the $(PP/Ce/GO/Ce)_{15}$/(DHI-melanin) film during depth profiling.

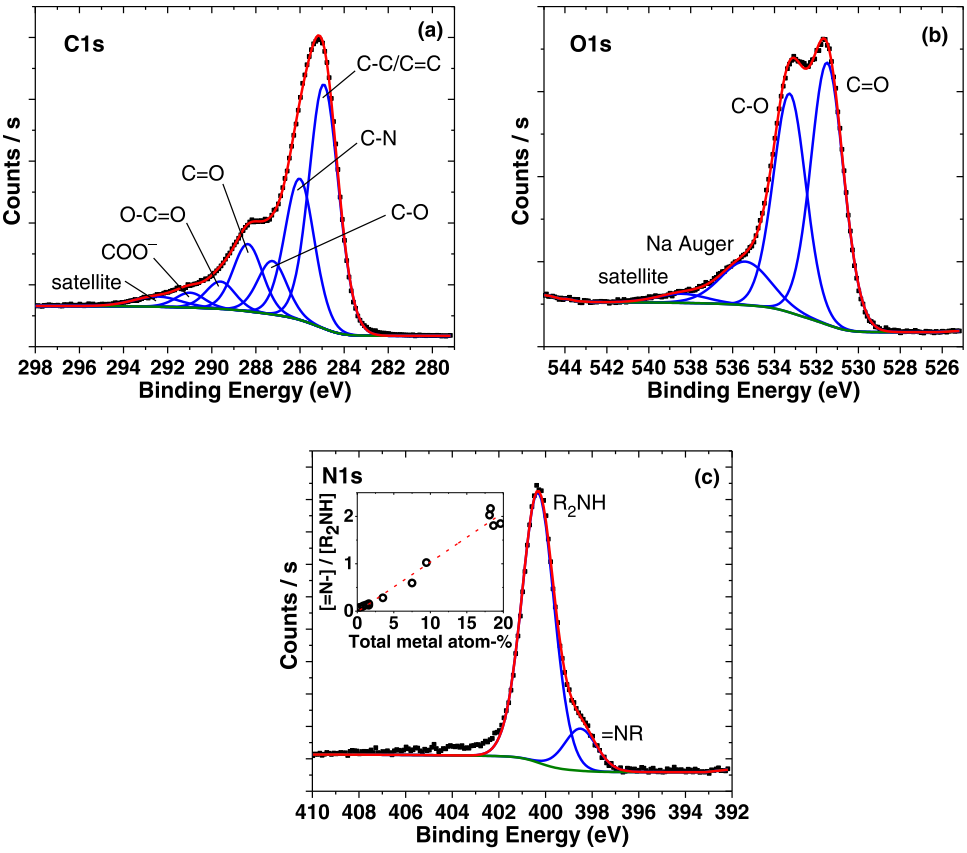

Figure 4. (a–c) C 1s, O 1s, and N 1s spectra of the $(PP/Ce/GO/Ce)_{15}$/(DHI-melanin) film after light sputtering for 40 s. The inset in (c) shows the dependence of the imine/amine ratio ([=N–] / [R_2NH]) on the total metal atom-% (Ce + Na) in the film (the dashed line is a linear fit to the data points).

catecholic form, both in the gas phase and in an aqueous solution.[37] On the other hand, IQ and QM are close in energy in vacuum,[37,38] likely due to intramolecular hydrogen bonding.[38] However, the *o*-quinone form IQ is more stable in water by many kJ mol^{-1},[37,38] and the other main tautomer of indolequinone, quinone imine QI, is even less stable than QM.[37,38] On the other hand, recent thermodynamic considerations suggest that, under the current conditions where the material is formed in a partially oxidized state at pH 4.5, QM may be present in similar amounts in aqueous solutions.[39] Therefore, DHI, QM, and IQ would be the main reduced and oxidized forms of the as-synthesized DHI-melanin.

In addition to carbon, oxygen, phosphorus, and cerium, the $(PP/Ce/GO/Ce)_{15}$/(DHI-melanin) film also contained nitrogen and sodium (Figures 3 and S3). Sodium is a remnant of

https://doi.org/10.1021/acsapm.2c01366
ACS Appl. Polym. Mater. XXXX, XXX, XXX−XXX

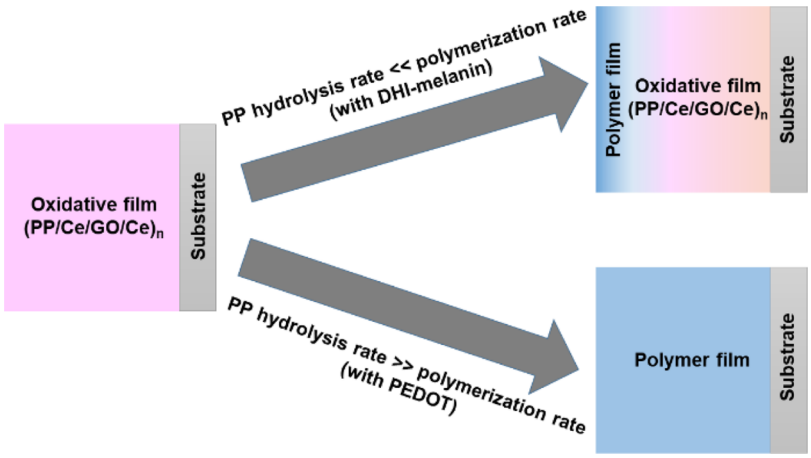

Figure 5. Role of polyphosphate hydrolysis during the monomer oxidation on the oxidative film. Film thicknesses shown are only schematic.

the buffer used in the polymerization. The atomic distributions display a marked depth dependence with the melanin-type material being concentrated close to the outer surface. Both cerium and polyphosphate were absent from this region, suggesting that DHI-melanin covers the whole surface, in accordance with our previous results.[5] The fraction of carbon and nitrogen (indicating the presence of melanin) dropped as the film was sputtered with a concomitant rise in the fraction of oxygen, phosphorus, and cerium (indicating the presence of the oxidative film). However, the removal of the DHI-melanin outer layer required longer sputtering times compared to PEDOT film (Figures 2 and 3), which implies stronger adhesion of the DHI-melanin coating.[25]

The structure of the oxidative multilayer was partially preserved in the bulk of the $(PP/Ce/GO/Ce)_{15}$/(DHI-melanin) film (Figure 3) but the Ce/P ratio was slightly smaller than in the bulk of a bare oxidative multilayer (ca. 2.1 and 2.7, respectively). Only little melanin-type material was found in the bulk both before (Figure 3) and after the electrochemical reduction of GO (Figure S10), as seen in the low amount of nitrogen, but some interpenetration down to the substrate surface takes place, as also evidenced by the electroactivity of the $(PP/Ce/rGO/Ce)_n$/(DHI-melanin) films (*vide infra*). The difference between the DHI-melanin and PEDOT-coated films is caused by the higher pH (4.5 vs 1.5) and shorter reaction time (2 vs 17 h) in the former case. Polyphosphate hydrolysis is markedly decreased under these conditions, and the oxidative film deterioration close to the outer surface is mostly caused by the low coordination capability of the Ce(III) ion formed. The DHI monomers cannot effectively enter the bulk of the multilayer either.

The $(PP/Ce/GO/Ce)_{15}$/(DHI-melanin) film was slightly cleaned by an argon gas cluster sputtering for 40 s to remove any possible impurities from the surface before recording the high-resolution XPS spectra in Figure 4 (see the Supporting Information for data of 0 s and 10 s sputtered film). The as-synthesized DHI-melanin is in a partially oxidized form and the C 1s spectra of the outer part of the film can be deconvoluted with four main peaks corresponding to C−C/C═C, C−N, C−O, and C═O carbons, and with three additional small peaks attributed to COOH, COO^-, and a satellite peak. The binding energies are generally in accordance with the literature[5,27,40] and the ratio of carbon functionalities is within the values anticipated for DHI-melanin, *e.g.*, close to the DHI_3/(pyrrole-2,3-dicarboxylic acid) tetramer[17,19] (Table S5). Relative areas of the carbon−nitrogen and carbon−oxygen peaks in the C 1s, O 1s, and N 1s spectra are also in good accordance with each other (Table S5). Transition-metal ions can enhance the intra- and extradiol cleavage of the catechol rings,[41] and the COOH groups formed in the ring cleavage act as a binding site for Na^+ ions.[42] Finally, the presence of the high-BE shake-up signal is confirmed by the reflection electron energy loss spectrum (REELS) of the film (Figure S13). The O 1s spectrum of the outer part of the film can be deconvoluted with two main peaks, C═O (531.5 eV) and C−O (533.3 eV),[5,27,40] together with a wide Na Auger and a satellite peak. It can be estimated that ca. 50% of the DHI-melanin is in the oxidized form.

The N 1s spectra of polydopamine have often been reported to contain a peak attributed to a primary amine ($R\text{-}NH_2$) or its protonated form ($R\text{-}NH_3^+$), with the binding energy of ca. 402 eV.[41] In all of these cases, the polydopamine film has been prepared by the oxidation of dopamine, and the amino functionality represents uncyclized monomers in the final product. On the other hand, in DHI-melanin films no free amino signal has been observed, and the major peak can be attributed to the pyrrolic nitrogen (R-NH-R) in the indole structure (400.3 eV).[5,27,40] Cleavage of the pyrrolic 5-ring can thus be ruled out. On the other hand, the minor component in the N 1s spectra at 398.5 eV was not observed in our previous work, probably due to the lower resolution of the spectra.[5] Calculations suggest that the QM form with a ═N− nitrogen group is present in DHI-melanin,[37−39] and we attribute the peak at 398.5 eV to the ═NR (imine group).[18,27,40] However, like Paulin et al., we observed that the ═NR/R_2NH group ratio increases significantly with film etching time.[27] The pK_a value of the secondary amine in IQ and DHI is most probably so high that the formation of an imino-like structure by deprotonation need not be considered. On the other hand, metal-ion binding is likely to affect the imine formation in DHI-melanin,[37,41] and the sputtering results offer now a direct way to study this hypothesis because the relative amount of cations, especially the cerium ions, increases with the film etching time (Figures 3, 4, S10, and S11). The presence of QM makes the imine/amine ratio nonzero even when no metal is present but the [═N−]/[R_2NH] ratio increases roughly linearly with metal content (Figures 4c and S11), which we attribute to the effect of metal coordination on the DHI form.

Overall, based on the results of this study, the polymer film formation mechanism on the oxidative multilayer can now be

https://doi.org/10.1021/acsapm.2c01366
ACS Appl. Polym. Mater. XXXX, XXX, XXX−XXX

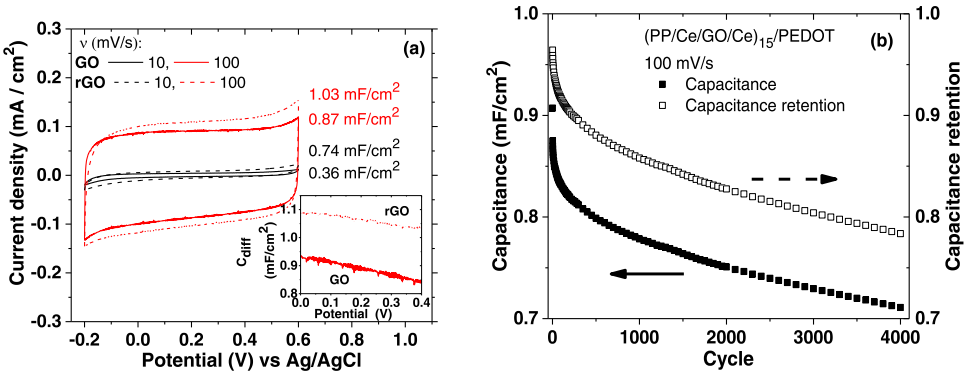

Figure 6. (a) Cyclic voltammograms of the $(PP/Ce/(r)GO/Ce)_{15}$/PEDOT electrode at 10 and 100 mV/s sweep rates (integrated capacitance values shown). The inset shows the differential capacitance (C_{diff}) as a function of potential (at 100 mV/s) for films with GO and rGO. (b) Capacitance retention of the $(PP/Ce/GO/Ce)_{15}$/PEDOT electrode as a function of charging−discharging cycles at 100 mV/s.

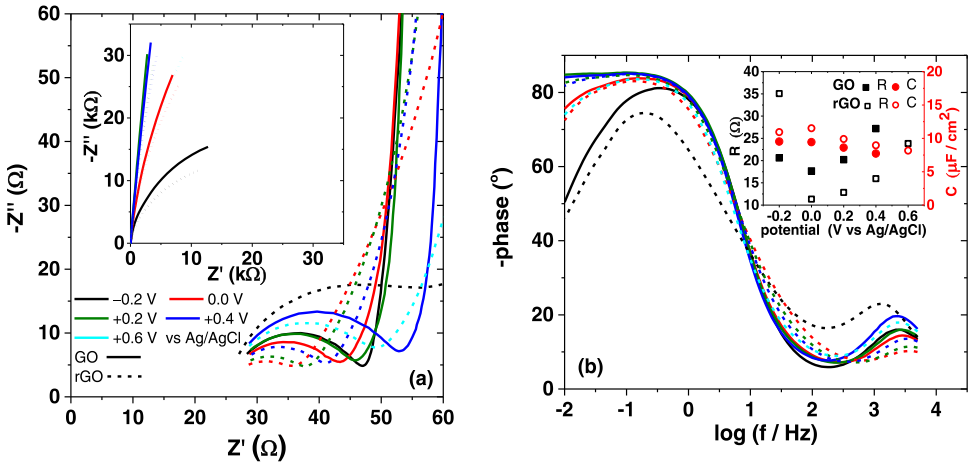

Figure 7. (a) High-frequency part of the Nyquist impedance plots of the $(PP/Ce/(r)GO/Ce)_{15}$/PEDOT electrode in 0.5 M Na_2SO_4 solution at different potentials (vs Ag/AgCl). The inset shows the whole frequency range. (b) Bode plots of the same electrode at different potentials. The inset shows the behavior of the capacitance and resistance attributed to the high-frequency semicircle as a function of potential.

explained. The polymer film formation on the oxidative multilayer takes place before the GO reduction. The SEM, XPS, and electrochemical studies of oxidative films in ferro/ferricyanide solution suggest that the monomers are unlikely to penetrate deep into the multilayer, and therefore, the reaction proceeds from the solution/multilayer interface (see the Supporting Information for details). However, during PEDOT film formation the polyphosphate hydrolysis takes place within the multilayer and PP and cerium are released as monomers are oxidized. Our earlier data show that Ce(IV) disappears from the film at approximately the same rate as PEDOT is formed, which supports this conclusion.[2] On the other hand, during the DHI-melanin formation, polyphosphate is not hydrolyzed to any significant degree, and the multilayer dissolution is mainly due to the lower complexing power of Ce(III). The bulk of the oxidative multilayer is stable and prevents DHI from entering deep inside it, which restricts the melanin formation mainly close to the multilayer/solution interface. Therefore, the decomposition of the oxidative multilayer concurrently with the monomer oxidation and subsequent reactions is favorable to the use of these LbL multilayers for polymer film formation (Figure 5). The reduction of GO is carried out after the film formation but the data presented suggest that this does not have a marked effect on the polymer film (Figure S10).

Capacitance of $(PP/Ce/(r)GO/Ce)_n$/PEDOT Films. The behavior of a $(PP/Ce/GO/Ce)_{15}$/PEDOT film was studied with electrochemical impedance spectroscopy (EIS) at different potentials between −0.2 V and +0.6 V (vs Ag/AgCl), both before and after the reduction of GO. The XPS results showed that this film consists only of PEDOT polymer and some graphene oxide sheets, with very little polyphosphate left, and it is homogeneous throughout its thickness. In addition, PEDOT in the film is in the oxidized state in the entire potential range[2] and the conductivity of the polymer increases with the potential.

The cyclic voltammograms of the $(PP/Ce/(r)GO/Ce)_{15}$/PEDOT film are shown in Figure 6a. The voltammograms are nearly rectangular in form, which is typical for capacitive behavior. The integrated capacitance clearly depends on the sweep rate, i.e., the experimental timescale, and the reduction of GO increases the capacitance. On the other hand, the differential capacitance decreases slightly with potential (inset of Figure 6a), as the cathodic and anodic current traces are not parallel. At 100 mV/s sweep rate, the initial integrated capacitance is ca. 0.9 mF/cm^2 with good charging−discharging stability. After the initial drop within the first 500 cycles, the capacitance decreases only ca. 2−4 percentage points/1000 cycles, and ca. 80% of the initial capacitance is retained after 4000 cycles, comparable with other PEDOT-based films (Figure 6b).[43,44]

https://doi.org/10.1021/acsapm.2c01366
ACS Appl. Polym. Mater. XXXX, XXX, XXX−XXX

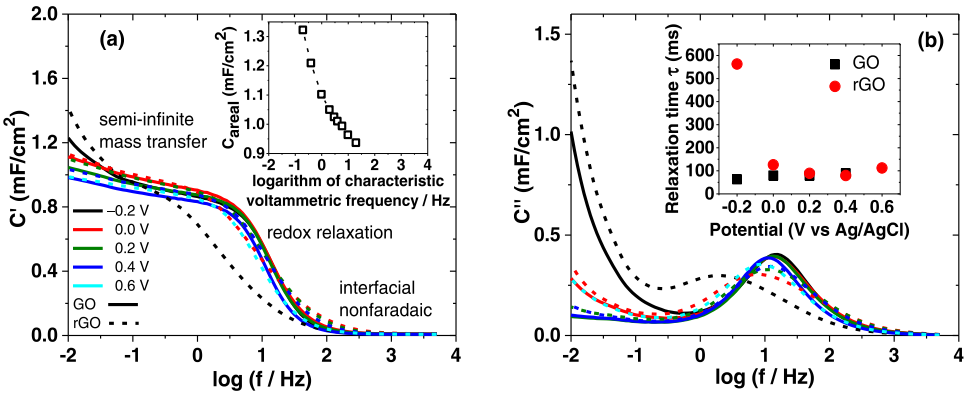

Figure 8. Real (a) and imaginary (b) parts of the complex capacitance as a function of frequency for the $(PP/Ce/(r)GO/Ce)_{15}$/PEDOT electrode in 0.5 M Na_2SO_4 at different potentials. The inset in (a) shows the voltammetrically obtained integrated areal capacitance of the $(PP/Ce/rGO/Ce)_{15}$/PEDOT as a function of the inverse of the voltammetric timescale ($=RT/Fv$). The inset in (b) shows the relaxation time corresponding to the maximum of C'' as a function of potential. The processes contributing to the film capacitance in different time domains are schematically shown in (a).

The impedance behavior of PEDOT films is quite complicated (Figure 7, see the SI for Kramers–Kronig test results for data quality validation), and is best described by a transmission line model and its modifications.[45] We do not consider that a quantitative analysis of the EIS results by equivalent circuits would markedly add to the understanding of the properties of the $(PP/Ce/(r)GO/Ce)_{15}$/PEDOT films. On the other hand, a qualitative inspection of the impedance spectra can lead to some physically important conclusions. At medium-to-low frequencies, the Nyquist plots display a gradual change from a nearly capacitive behavior toward a diffusion-controlled domain. This behavior is qualitatively similar to that on a pseudocapacitive electrode, and the phase angle in this frequency range is close to a purely capacitive behavior.[46] The reduction of GO slightly increases the nonideal behavior of the film at the lowest frequencies, which can be attributed to the morphological changes involved.

At high frequencies, the Nyquist plots show a semicircle-like feature (a hump in the Bode plots), which is not usually observed in the impedance spectra of PEDOT films, except sometimes in nonaqueous solutions.[47,48] Such a semicircle is often attributed to the interfacial charge transfer resistance, or to the interfacial impedance at the electrode/film interface.[46] The simplest model for a capacitive interface consists of a parallel double-layer capacitor C_{dl} and a parallel resistance R_p in series with a solution/electrode resistance.[49] This model describes the semicircles in the Nyquist plots rather well (Figure S20 and Table S8), and the resulting capacitance and parallel resistance values are shown in the inset of Figure 7b at different potentials before and after the GO reduction. This capacitance is negligible compared to the observed total integrated capacitance (Figure 6), and it is quite insensitive to the applied potential and the state of GO in the film, but the parallel resistance shows a minimum and decreases upon the GO reduction (except at the lowest potential). This resistance determines the leakage current through the interface at the time domain corresponding to these high frequencies. Its complex behavior as a function of potential and GO redox state cannot be unambiguously interpreted, and as seen below, it is not relevant to the overall properties of the capacitive film. We can tentatively attribute the behavior to changes in the film conductivity and the morphological changes upon the GO reduction and PEDOT film swelling during its doping.

The impedance spectroscopy commonly used in electrochemistry is only one form of the general immittance spectroscopy. In studies of system dynamics, another form, called capacitance spectroscopy, can offer certain advantages over the EIS. Capacitance spectroscopy is a model-independent tool that yields information about the charge transfer kinetics and other dynamic processes.[50,51] The complex capacitance is defined as $C(\omega) = 1/(j\omega Z(\omega))$, where j is the imaginary unit, and $\omega = 2\pi f$ the angular frequency. The real C' and imaginary C'' parts of it are obtained from the impedance data according to eqs 1 and 2, where $Z' = Z'_{obs} - R_s$ (R_s = solution and electrode resistance (26 Ω), which is usually subtracted from the observed impedance)[50,51]

$$C' = -\frac{Z''}{2\pi f|Z|^2} \quad (1)$$

$$C'' = \frac{Z'}{2\pi f|Z|^2} \quad (2)$$

The complex capacitance is directly related to the complex dielectric function and yields information about any relaxation processes in the system.[52] The real part is related to the film capacitance and the imaginary part to conductivity and energy loss terms.[53] Figure 8 shows the real and imaginary components of the complex capacitance of the $(PP/Ce/(r)GO/Ce)_{15}$/PEDOT film as a function of excitation frequency at different potentials. At low frequencies, the real part of the complex capacitance C' is of the order of 1 mF/cm², in line with the integrated capacitance value, and decreases slightly with potential. This is in accordance with the differential capacitance, which is seen to decrease with potential (Figure 6a).

The imaginary component C'' represents the frequency dependence of all kinds of relaxation phenomena at the electrode.[50] Figure 8b shows that C'' displays a clear maximum at around 10 Hz, concurrent with a large drop in C', nearly independent of the GO reduction and electrode potential, except at the most cathodic potential (Table S9). To unambiguously differentiate between relaxation due to redox reactions and other processes the capacitance spectrum should be measured at potentials where PEDOT is not electroactive.[51] This is not feasible in this case as it would require exposing the

https://doi.org/10.1021/acsapm.2c01366
ACS Appl. Polym. Mater. XXXX, XXX, XXX–XXX

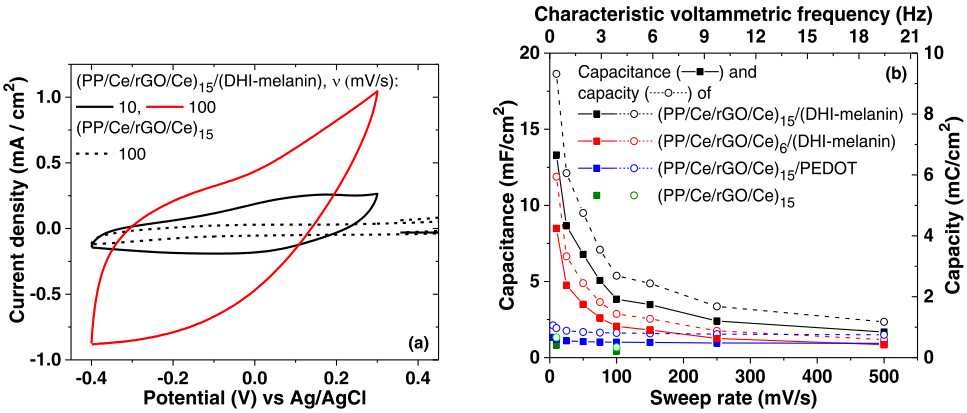

Figure 9. (a) Cyclic voltammograms of the $(PP/Ce/rGO/Ce)_{15}$ (in 0.5 M Na_2SO_4) and $(PP/Ce/rGO/Ce)_{15}$/(DHI-melanin) films (in 0.1 M phosphate buffer with 0.5 M Na_2SO_4, pH = 7.1). (b) Capacitance and the charge storage capacity of the $(PP/Ce/rGO/Ce)_{15}$, $(PP/Ce/rGO/Ce)_{15}$/PEDOT, and $(PP/Ce/rGO/Ce)_n$/(DHI-melanin) films with different sweep rates (n = 6 or 15). Data for $(PP/Ce/rGO/Ce)_{15}$ and $(PP/Ce/rGO/Ce)_{15}$/PEDOT films have been taken from our earlier work.[2]

film to very cathodic potentials for a longer time. However, the high-frequency edge of the C'' peak coincides with the low-frequency end of the semicircle in the Nyquist plots, as clearly seen when comparing Figure 8b and the Bode plots in Figure 7b, and the peak maximum is well in the rising part of the Nyqvist plot, attributed to the pseudocapacitive behavior of the film in the form of redox reactions.[46] Therefore, we can attribute the C'' maximum to charge transfer phenomena.[54] The analysis of the Nyquist plots suggested that the high-frequency semicircle is due to interfacial nonfaradaic processes, which conclusion is further supported by the capacitance plots. The behavior of the high-frequency parts of the C' and C'' plots (corresponding to the frequencies of the semicircles in the Nyquist plots) does not follow that expected for a relaxation process but is in accordance with the model of interfacial nonfaradaic phenomena (see the SI for details). These high-frequency phenomena have only a negligible effect on the overall capacitive behavior of the film.

We can, therefore, elaborate our earlier conclusions about the source of the (r)GO/PEDOT film capacitance.[2] At long timescales, the small intrinsic electrical double-layer capacitance of the film (passive capacitance, seen at high frequencies; Figures 8a and S21) and the charge transfer (active) redox pseudocapacitance, mechanistically due to the charging/discharging of the nanocapacitors consisting of the polymer and counterions (seen at low−medium frequencies; Figures 8a and S21), both contribute to the observed capacitance. However, when the timescale becomes smaller the transfer processes have no time to contribute, which leads to a decrease in the observed capacitance and is clearly seen in the previously reported scan rate dependence of the (r)GO/PEDOT film capacitance.[2] If the characteristic voltammetric timescale[55] is taken as $(\tau = RT)/Fv$ we can define a voltammetric frequency scale as $f = 1/\tau$. This approximate analysis allows us to compare the voltammetric and impedance results, showing that the drop in the integrated capacitance takes place at frequencies close to the C'' peak (inset of Figure 8a). The anomalous effect of the GO reduction at −0.2 V vs Ag/AgCl is significant only at very low frequencies below 0.1 Hz, in which timescale we can expect diffusional mass transfer control to be important. The conductivity of the film is also low at this potential, decreasing the contribution from redox processes and emphasizing passive double-layer charging.

The time constant τ corresponding to the maximum of C'' is often used as a figure of merit for supercapacitors because it is directly related to the effective discharge rate, and therefore the power density, of the capacitor.[50,56,57] Except for the rGO-containing film at the lowest potential the time constant is (90 ± 20) ms (inset of Figure 8b and Table S9; the error refers to the standard deviation of data). It is practically independent of the redox state of GO in the film, which is understandable because (r)GO is only a minor component in the film. This value is very small in comparison to many other capacitive films based on carbonaceous materials or polythiophenes and their composites.[50,56−62]

Capacitance of $(PP/Ce/rGO/Ce)_n$/(DHI-melanin) Films. Our aim is to create biodegradable supercapacitors for transient electronics, and although the biocompatibility of PEDOT is relatively good,[10,11,63] it is not an ideal material for this purpose. Bioinspired materials would be desirable, and melanins and other quinonoid compounds have recently attracted attention as versatile and cost-effective bioinspired alternatives for supercapacitor electrode materials.[13−15,64]

The electrochemical reduction of GO (Figure S24) significantly enhances the electroactivity of the $(PP/Ce/GO/Ce)_n$/(DHI-melanin) films, and all electrochemical measurements were performed after the reduction. Cyclic voltammograms of the $(PP/Ce/rGO/Ce)_n$/(DHI-melanin) films are shown in Figures 9a and S23, using a rather small potential range because of the irreversible changes in the DHI-melanin at higher anodic potentials in aqueous media.[5,24] The voltammograms do not show any specific redox process in the studied potential range, which is typical to the DHI-melanin,[14,65] even though its oxidation state changes continuously within the whole potential window.[5] This can be attributed to the convolution of several redox processes of various redox pairs in different chemical environments.[13]

The areal capacitance and charge storage capacity of the $(PP/Ce/rGO/Ce)_n$/(DHI-melanin) films strongly depend on the timescale of the experiment, and they are compared to the corresponding values of the $(PP/Ce/rGO/Ce)_{15}$/PEDOT and $(PP/Ce/rGO/Ce)_{15}$ films in Figure 9b (the upper axis shows the characteristic voltammetric frequency to allow comparison with the PEDOT films). Both the areal capacitance and capacity of the $(PP/Ce/rGO/Ce)_{15}$/(DHI-melanin) films are much higher than those of the $(PP/Ce/rGO/Ce)_{15}$/PEDOT film, especially at low sweep rates. However, they decrease

https://doi.org/10.1021/acsapm.2c01366
ACS Appl. Polym. Mater. XXXX, XXX, XXX−XXX

rapidly with the sweep rate, which is unfortunately typical for melanin-based electrodes.[13,65] On the other hand, the areal capacitance and capacity still remain higher than with PEDOT-based films in the entire sweep rate range studied. This shows that melanin-based materials have a good potential for efficient biocompatible supercapacitor films but the dynamic properties of the studied films are not optimal. We envision that the charge transfer kinetics of the material can be improved by mixing DHI-melanin and materials with higher electronic conductivity,[35] or by using alternative deposition methods that are currently being investigated. In fact, the present work has shown that the oxidative LbL multilayers are not optimally suited for the deposition of DHI-melanin films because the intact multilayer beneath the polymer film greatly increases electrode resistance. However, the oxidative multilayers can produce high-quality PEDOT films.

Finally, it may be noted that, outside the potential window used for the capacitance measurements, the voltammograms of $(PP/Ce/rGO/Ce)_n$/(DHI-melanin) have a distinctive feature, an evident redox peak pair at ca. −0.85 V during the reduction of GO (Figure S24). This peak is observed at slightly more cathodic potentials than the oxidation−reduction peaks of the $[Ce(catecholate)_4]^{4-}$ complex or related compounds,[66,67] and we attribute the observed redox peaks to the Ce(III)/Ce(IV)—DHI-melanin complexes in the film. The cathodic peak current (Figure S24) is clearly higher than the anodic one, suggesting that the Ce(III) DHI-melanin complex is much less stable and more prone to side reactions.[67] It is noteworthy that in the oxidative films the Ce(III)/Ce(IV) redox pair is typically sluggish[3,4] and these redox peaks were not observed in the reduction voltammogram of the bare oxidative $(PP/Ce/GO/Ce)_{15}$ film (data not shown). However, this redox process is not relevant to the use of these films in capacitors, except that they show the presence of electroactive cerium species in the films.

CONCLUSIONS

Oxidative multilayers prepared by sequential layer-by-layer deposition using polyphosphate (PP), Ce(IV), and graphene oxide (GO) provide an effective electrodeless method to form electroactive and capacitive polymer films on spatially defined areas. It has been known that in these multilayers Ce(IV) acts as an oxidant and GO enhances the multilayer growth and its mechanical properties. In this work, we have shown that PP is an essential component that binds the multilayer together, and it is hydrolyzed under acidic conditions by a random cleavage of the P−O−P bonds in the linear chain. This mechanism rapidly decreases the mean polymer chain length, which leads to the dissolution of the multilayer, especially when Ce(IV) has been converted to less coordinating Ce(III) during the polymerization reactions. This happens with conducting polymers, e.g., PEDOT, when polymerized at low pH. However, this seems to be advantageous because, in spite of the multilayer dissolution, the process leads to a homogeneous polymer film well attached to the substrate and removes most of the bioincompatible cerium from the film. The so-formed PEDOT film is thinner than the original oxidative multilayer and consists mainly of the polymer with a small amount of GO (ca. 80% w/w PEDOT) but only negligible amounts of cerium or PP. This guarantees a good-quality conducting film with direct electrical contact with the substrate electrode. On the other hand, in the case of DHI-melanin formation the reaction time is too short and the pH too high for a significant PP hydrolysis to take place. Therefore, DHI-melanin film is mainly formed only on the exterior surface of the oxidative multilayer while the bulk of the multilayer remains intact. This severely weakens the electrical contact between the redox-active melanin-type film and results in a long time constant for electrochemical processes. In general, the oxidative multilayers produce good-quality polymer films when the PP hydrolysis rate is much faster than the polymerization rate.

The formed PEDOT films possess good specific volumetric and mass capacitance, which are well retained after successive charging−discharging cycles. We have used capacitance spectroscopy to identify various dynamic processes that contribute to the capacitance and the electrochemical behavior of the film in general. The analysis shows that interfacial capacitance, redox pseudocapacitance, and mass transfer effects all contribute to the observed capacitance at different timescales and experimental frequencies. The interfacial capacitance is effective at high frequencies, but its contribution is negligible to the capacitance observed at voltammetric timescales. The main contribution at voltammetric timescale comes from redox processes, which therefore pose the ultimate limitation for the power density of the capacitive film. The DHI-melanin films, on the other hand, have still higher areal capacitance than the PEDOT films. The observed capacitance decreases rapidly with decreasing timescale, however always staying greater than that of the PEDOT film.

Fabricating melanin-type capacitive films suitable for biodegradable supercapacitors requires improving the properties of the current films, although their energy density seems promising. In this respect, two factors must be specifically addressed. Using oxidative films is not a suitable technique to prepare these films because the melanin-type material is concentrated on the outer surface of the multilayer. The nearly intact nonconducting multilayer between the redox-active layer and the electrode greatly increases the film time constant, thereby effectively decreasing the power density of the film. This calls for alternative methods of film preparation, which is not straightforward with these generally intractable materials, that would also eliminate the use of a bioincompatible metal like cerium. On the other hand, the conductivity of the melanin-type material must also be increased, and the film fabrication technique should have high material and cost efficiency, and be sustainable and upscalable. We are currently addressing these questions in our present ongoing work.

ASSOCIATED CONTENT

Supporting Information

The Supporting Information is available free of charge at https://pubs.acs.org/doi/10.1021/acsapm.2c01366.

Additional experimental details; ^{31}P NMR analysis of polyphosphate; kinetic model of polyphosphate hydrolysis; XPS, SEM, EDS, and AFM analysis of the $(PP/Ce/GO/Ce)_{15}$, $(PP/Ce/GO/Ce)_{15}$/PEDOT, and $(PP/Ce/GO/Ce)_{15}$/(DHI-melanin) films; detailed analysis of the Ce 3d XPS spectra; REELS analysis of the $(PP/Ce/GO/Ce)_{15}$, $(PP/Ce/GO/Ce)_{15}$/PEDOT, and $(PP/Ce/GO/Ce)_{15}$/(DHI-melanin) films; scanning white light interferometry image of the $(PP/Ce/rGO/Ce)_{15}$/(DHI-melanin) film; electrochemistry of the $(PP/Ce/(r)GO/Ce)_{15}$, $(PP/Ce/(r)GO/Ce)_{15}$/PEDOT, and $(PP/Ce/rGO/Ce)_n$/(DHI-melanin) films; electrochem-

https://doi.org/10.1021/acsapm.2c01366
ACS Appl. Polym. Mater. XXXX, XXX, XXX−XXX

ical reduction of graphene oxide; and Kramers−Kronig tests of the impedance data (PDF)

AUTHOR INFORMATION

Corresponding Authors

Lauri Marttila − *Department of Chemistry and The Doctoral Programme in Exact Sciences, University of Turku, FI-20500 Turku, Finland;* orcid.org/0000-0002-8221-0954; Email: ljmart@utu.fi

Mikko Salomäki − *Department of Chemistry and Turku University Centre for Materials and Surfaces (MatSurf), University of Turku, FI-20500 Turku, Finland;* orcid.org/0000-0001-6190-2073; Email: mikko.salomaki@utu.fi

Jukka Lukkari − *Department of Chemistry and Turku University Centre for Materials and Surfaces (MatSurf), University of Turku, FI-20500 Turku, Finland;* orcid.org/0000-0002-9409-7995; Email: jukka.lukkari@utu.fi

Authors

Henri Kivelä − *Department of Chemistry and Turku University Centre for Materials and Surfaces (MatSurf), University of Turku, FI-20500 Turku, Finland;* orcid.org/0000-0003-1414-8893

Jukka Hassinen − *Department of Chemistry, University of Turku, FI-20500 Turku, Finland;* Present Address: Department of Bioproducts and Biosystems, Aalto University, FI-00076 Espoo, Finland; orcid.org/0000-0002-4167-4269

Sari Granroth − *Department of Physics and Astronomy and Turku University Centre for Materials and Surfaces (MatSurf), University of Turku, FI-20500 Turku, Finland*

Ermei Mäkilä − *Department of Physics and Astronomy and The Doctoral Programme in Exact Sciences, University of Turku, FI-20500 Turku, Finland;* orcid.org/0000-0002-8300-6533

Johan Nyman − *Pharmaceutical Sciences Laboratory, Faculty of Science and Engineering, Åbo Akademi University, 20520 Turku, Finland*

Complete contact information is available at: https://pubs.acs.org/10.1021/acsapm.2c01366

Author Contributions

L.M. wrote the draft of the manuscript, and L.M. and J.L. are the main authors. L.M. performed most of the experimental work and participated in data analysis. M.S. supervised most of the experimental work, J.H. carried out the polyphosphate NMR analysis, H.K. participated in the supervision and NMR analysis, S.G. supervised the XPS measurements, E.M. carried out the SEM and EDS measurements, and J.N. the SWLI measurements.

Funding

L.M. gratefully acknowledges the Emil Aaltonen Foundation (grant number 180162 N), the Finnish Cultural Foundation (grant number 00210708), and Foundation of Finnish Chemistry Congress for research grants.

Notes

The authors declare no competing financial interest.

ACKNOWLEDGMENTS

The authors are grateful to Milla Suominen, Sachin Kochrekar, and Adefunke Koyejo for their participation in the synthesis of graphene oxide. J.L. wishes to thank his late mother, Dr. Helvi Lukkari (1924−2022), for all her support.

REFERENCES

(1) *Multilayer Thin Films: Sequential Assembly of Nanocomposite Materials*, 2nd ed.; Decher, G.; Schlenoff, J. B., Eds.; Wiley, 2012 DOI: 10.1002/9783527646746.

(2) Salomäki, M.; Marttila, L.; Kivelä, H.; Tupala, M.; Lukkari, J. Oxidative Spin-Spray-Assembled Coordinative Multilayers as Platforms for Capacitive Films. *Langmuir* **2020**, *36*, 6736−6748.

(3) Salomäki, M.; Räsänen, M.; Leiro, J.; Huti, T.; Tenho, M.; Lukkari, J.; Kankare, J. Oxidative Inorganic Multilayers for Polypyrrole Film Generation. *Adv. Funct. Mater.* **2010**, *20*, 2140−2147.

(4) Salomäki, M.; Myllymäki, O.; Hätönen, M.; Savolainen, J.; Lukkari, J. Layer-by-Layer Assembled Oxidative Films as General Platform for Electrodeless Formation of Conducting Polymers. *ACS Appl. Mater. Interfaces* **2014**, *6*, 2325−2334.

(5) Salomäki, M.; Tupala, M.; Parviainen, T.; Leiro, J.; Karonen, M.; Lukkari, J. Preparation of Thin Melanin-Type Films by Surface-Controlled Oxidation. *Langmuir* **2016**, *32*, 4103−4112.

(6) Salomäki, M.; Kauppila, J.; Kankare, J.; Lukkari, J. Oxidative Layer-By-Layer Multilayers Based on Metal Coordination: Influence of Intervening Graphene Oxide Layers. *Langmuir* **2018**, *34*, 13171−13182.

(7) Najib, S.; Erdem, E. Current Progress Achieved in Novel Materials for Supercapacitor Electrodes: Mini Review. *Nanoscale Adv.* **2019**, *1*, 2817−2827.

(8) Li, R.; Wang, L.; Kong, D.; Yin, L. Recent Progress on Biodegradable Materials and Transient Electronics. *Bioact. Mater.* **2018**, *3*, 322−333.

(9) Hosseini, E. S.; Dervin, S.; Ganguly, P.; Dahiya, R. Biodegradable Materials for Sustainable Health Monitoring Devices. *ACS Appl. Bio Mater.* **2021**, *4*, 163−194.

(10) Boehler, C.; Aqrawe, Z.; Asplund, M. Applications of PEDOT in Bioelectronic Medicine. *Bioelectron. Med.* **2019**, *2*, 89−99.

(11) Asplund, M.; Thaning, E.; Lundberg, J.; Sandberg-Nordqvist, A. C.; Kostyszyn, B.; Inganäs, O.; von Holst, H. Toxicity Evaluation of PEDOT/Biomolecular Composites Intended for Neural Communication Electrodes. *Biomed. Mater.* **2009**, *4*, No. 045009.

(12) Sim, H. J.; Choi, C.; Lee, D. Y.; Kim, H.; Yun, J.-H.; Kim, J. M.; Kang, T. M.; Ovalle, R.; Baughman, R. H.; Kee, C. W.; Kim, S. J. Biomolecule Based Fiber Supercapacitor for Implantable Device. *Nano Energy* **2018**, *47*, 385−392.

(13) Kumar, P.; Di Mauro, E.; Zhang, S.; Pezzella, A.; Soavi, F.; Santato, C.; Cicoira, F. Melanin-Based Flexible Supercapacitors. *J. Mater. Chem. C* **2016**, *4*, 9516−9525.

(14) Xu, R.; Gouda, A.; Caso, M. F.; Soavi, F.; Santato, C. Melanin: A Greener Route To Enhance Energy Storage under Solar Light. *ACS Omega* **2019**, *4*, 12244−12251.

(15) Gouda, A.; Masson, A.; Hoseinizadeh, M.; Soavi, F.; Santato, C. Biosourced Quinones for High-Performance Environmentally Benign Electrochemical Capacitors via Interface Engineering. *Commun. Chem.* **2022**, *5*, No. 98.

(16) Mostert, A. B. Melanin, the What, the Why and the How: An Introductory Review for Materials Scientists Interested in Flexible and Versatile Polymers. *Polymers* **2021**, *13*, 1670.

(17) Alfieri, M. L.; Micillo, R.; Panzella, L.; Crescenzi, O.; Oscurato, S. L.; Maddalena, P.; Napolitano, A.; Ball, V.; d'Ischia, M. Structural Basis of Polydopamine Film Formation: Probing 5,6-Dihydroxyindole-Based Eumelanin Type Units and the Porphyrin Issue. *ACS Appl. Mater. Interfaces* **2018**, *10*, 7670−7680.

(18) Lyu, Q.; Hsueh, N.; Chai, C. L. L. Direct Evidence for the Critical Role of 5,6-Dihydroxyindole in Polydopamine Deposition and Aggregation. *Langmuir* **2019**, *35*, 5191−5201.

(19) Della Vecchia, N. F.; Avolio, R.; Alfè, M.; Errico, M. E.; Napolitano, A.; d'Ischia, M. Building-Block Diversity in Polydopamine Underpins a Multifunctional Eumelanin-Type Platform

Tunable Through a Quinone Control Point. *Adv. Funct. Mater.* **2013**, *23*, 1331−1340.
(20) Lyu, Q.; Song, H.; Yakovlev, N. L.; Tan, W. S.; Chai, C. L. L. *In Situ* Insights into the Nanoscale Deposition of 5,6-Dihydroxyindole-Based Coatings and the Implications on the Underwater Adhesion Mechanism of Polydopamine Coatings. *RSC Adv.* **2018**, *8*, 27695−27702.
(21) Lee, H.; Dellatore, S. M.; Miller, W. M.; Messersmith, P. B. Mussel-Inspired Surface Chemistry for Multifunctional Coatings. *Science* **2007**, *318*, 426−430.
(22) Bloisi, F.; Pezzella, A.; Barra, M.; Alfè, M.; Chiarella, F.; Cassinese, A.; Vicari, L. Effect of Substrate Temperature on MAPLE Deposition of Synthetic Eumelanin Films. *Appl. Phys. A: Mater. Sci. Process.* **2011**, *105*, 619−627.
(23) Horak, V.; Weeks, G. Poly(5,6-dihydroxyindole) Melanin Film Electrode. *Bioorg. Chem.* **1993**, *21*, 24−33.
(24) Stark, K. B.; Gallas, J. M.; Zajac, G. W.; Golab, J. T.; Gidanian, S.; McIntire, T.; Farmer, P. J. Effect of Stacking and Redox State on Optical Absorption Spectra of Melanins−Comparison of Theoretical and Experimental Results. *J. Phys. Chem. B* **2005**, *109*, 1970−1977.
(25) Pezzella, A.; Barra, M.; Musto, A.; Navarra, A.; Alfè, M.; Manini, P.; Parisi, S.; Cassinese, A.; Criscuolo, V.; d'Ischia, M. Stem Cell-Compatible Eumelanin Biointerface Fabricated by Chemically Controlled Solid State Polymerization. *Mater. Horiz.* **2015**, *2*, 212−220.
(26) Yun, D.-J.; Chung, J.; Kim, S. H.; Kim, Y.; Seol, M.; Chung, J.; Park, S.-H. Study on the Molecular Distribution of Organic Composite Films by Combining Photoemission Spectroscopy with Argon Gas Cluster Ion Beam Sputtering. *J. Mater. Chem. C* **2015**, *3*, 276−282.
(27) Paulin, J. V.; McGettrick, J. D.; Graeff, C. F. O.; Mostert, A. B. Melanin System Composition Analyzed by XPS Depth Profiling. *Surf. Interfaces* **2021**, *24*, No. 101053.
(28) Brown, M. R. W.; Kornberg, A. Inorganic Polyphosphate in the Origin and Survival of Species. *Proc. Natl. Acad. Sci. U.S.A.* **2004**, *101*, 16085−16087.
(29) Rao, N. N.; Gómez-García, M. R.; Kornberg, A. Inorganic Polyphosphate: Essential for Growth and Survival. *Annu. Rev. Biochem.* **2009**, *78*, 605−647.
(30) Kornberg, A.; Rao, N. N.; Ault-Riché, D. Inorganic Polyphosphate: A Molecule of Many Functions. *Annu. Rev. Biochem.* **1999**, *68*, 89−125.
(31) Kornberg, A. Inorganic Polyphosphate: Toward Making a Forgotten Polymer Unforgettable. *J. Bacteriol.* **1995**, *177*, 491−496.
(32) Omelon, S. J.; Grynpas, M. D. Relationships between Polyphosphate Chemistry, Biochemistry and Apatite Biomineralization. *Chem. Rev.* **2008**, *108*, 4694−4715.
(33) de Jager, H.-J.; Heyns, A. M. Kinetics of Acid-Catalyzed Hydrolysis of a Polyphosphate in Water. *J. Phys. Chem. A* **1998**, *102*, 2838−2841.
(34) Kawabe, M.; Ohashi, O.; Yamaguchi, I. Phosphorus Nuclear Magnetic Resonance in Polyphosphates and Determination of Their Hydrolysis Rate Constants. *Bull. Chem. Soc. Jpn.* **1970**, *43*, 3705−3710.
(35) Gargiulo, V.; Alfè, M.; Capua, R. D.; Togna, A. R.; Cammisotto, V.; Fiorito, S.; Musto, A.; Navarra, A.; Parisi, S.; Pezzella, A. Supplementing π-Systems: Eumelanin and Graphene-like Integration towards Highly Conductive Materials for the Mammalian Cell Culture Bio-Interface. *J. Mater. Chem. B* **2015**, *3*, 5070−5079.
(36) Moraes, F. C.; Freitas, R. G.; Pereira, R.; Gorup, L. F.; Cuesta, A.; Pereira, E. C. Coupled Electronic and Morphologic Changes in Graphene Oxide upon Electrochemical Reduction. *Carbon* **2015**, *91*, 11−19.
(37) Il'ichev, Y. V.; Simon, J. D. Building Blocks of Eumelanin: Relative Stability and Excitation Energies of Tautomers of 5,6-Dihydroxyindole and 5,6-Indolequinone. *J. Phys. Chem. B* **2003**, *107*, 7162−7171.
(38) Pezzella, A.; Crescenzi, O.; Panzella, L.; Napolitano, A.; Land, E. J.; Barone, V.; d'Ischia, M. Free Radical Coupling of *o*-Semiquinones Uncovered. *J. Am. Chem. Soc.* **2013**, *135*, 12142−12149.
(39) Mostert, A. B. On the Free Radical Redox Chemistry of 5,6-Dihydroxyindole. *Chem. Phys.* **2021**, *546*, No. 111158.
(40) Clark, M. B.; Gardella, J. A.; Schultz, T. M.; Patil, D. G.; Salvati, L. Solid-State Analysis of Eumelanin Biopolymers by Electron Spectroscopy for Chemical Analysis. *Anal. Chem.* **1990**, *62*, 949−956.
(41) Salomäki, M.; Ouvinen, T.; Marttila, L.; Kivelä, H.; Leiro, J.; Mäkilä, E.; Lukkari, J. Polydopamine Nanoparticles Prepared Using Redox-Active Transition Metals. *J. Phys. Chem. B* **2019**, *123*, 2513−2524.
(42) Hong, L.; Simon, J. D. Current Understanding of the Binding Sites, Capacity, Affinity, and Biological Significance of Metals in Melanin. *J. Phys. Chem. B* **2007**, *111*, 7938−7947.
(43) Mao, X.; Yang, W.; He, X.; Chen, Y.; Zhao, Y.; Zhou, Y.; Yang, Y.; Xu, J. The Preparation and Characteristic of Poly (3,4-ethylenedioxythiophene)/Reduced Graphene Oxide Nanocomposite and Its Application for Supercapacitor Electrode. *Mater. Sci. Eng., B* **2017**, *216*, 16−22.
(44) Chen, Y.; Xu, J.; Mao, Y.; Yang, Y.; Yang, W.; Li, S. Electrochemical Performance of Graphene-Polyethylenedioxythiophene Nanocomposites. *Mater. Sci. Eng., B* **2013**, *178*, 1152−1157.
(45) Kayinamura, Y. P.; Ovadia, M.; Zavitz, D.; Rubinson, J. F. Investigation of Near Ohmic Behavior for Poly(3,4-Ethylenedioxythiophene): A Model Consistent with Systematic Variations in Polymerization Conditions. *ACS Appl. Mater. Interfaces* **2010**, *2*, 2653−2662.
(46) Mathis, T. S.; Kurra, N.; Wang, X.; Pinto, D.; Simon, P.; Gogotsi, Y. Energy Storage Data Reporting in Perspective-Guidelines for Interpreting the Performance of Electrochemical Energy Storage Systems. *Adv. Energy Mater.* **2019**, *9*, No. 1902007.
(47) Bobacka, J. Potential Stability of All-Solid-State Ion-Selective Electrodes Using Conducting Polymers as Ion-to-Electron Transducers. *Anal. Chem.* **1999**, *71*, 4932−4937.
(48) Sundfors, F.; Gustafsson, H.; Ivaska, A.; Kvarnström, C. Characterisation of the Aluminium−Electropolymerised Poly(3,4-Ethylenedioxythiophene) System. *J. Solid State Electrochem.* **2010**, *14*, 1185−1195.
(49) Zhao, X.; Aoki, K. J.; Chen, J.; Nishiumi, T. Examination of the Gouy−Chapman Theory for Double Layer Capacitance in Deionized Latex Suspensions. *RSC Adv.* **2014**, *4*, 63171−63181.
(50) Taberna, P. L.; Simon, P.; Fauvarque, J. F. Electrochemical Characteristics and Impedance Spectroscopy Studies of Carbon-Carbon Supercapacitors. *J. Electrochem. Soc.* **2003**, *150*, A292.
(51) Bueno, P. R.; Mizzon, G.; Davis, J. J. Capacitance Spectroscopy: A Versatile Approach To Resolving the Redox Density of States and Kinetics in Redox-Active Self-Assembled Monolayers. *J. Phys. Chem. B* **2012**, *116*, 8822−8829.
(52) Góes, M. S.; Rahman, H.; Ryall, J.; Davis, J. J.; Bueno, P. R. A Dielectric Model of Self-Assembled Monolayer Interfaces by Capacitive Spectroscopy. *Langmuir* **2012**, *28*, 9689−9699.
(53) Bueno, P. R.; Varela, J. A.; Longo, E. Admittance and Dielectric Spectroscopy of Polycrystalline Semiconductors. *J. Eur. Ceram. Soc.* **2007**, *27*, 4313−4320.
(54) Mei, B.-A.; Lau, J.; Lin, T.; Tolbert, S. H.; Dunn, B. S.; Pilon, L. Physical Interpretations of Electrochemical Impedance Spectroscopy of Redox Active Electrodes for Electrical Energy Storage. *J. Phys. Chem. C* **2018**, *122*, 24499−24511.
(55) Amatore, C.; Maisonhaute, E. When Voltammetry Reaches Nanoseconds. *Anal. Chem.* **2005**, *77*, 303 A−311 A.
(56) Kumar, A.; Kumar, N.; Sharma, Y.; Leu, J.; Tseng, T. Y. Synthesis of Free-Standing Flexible RGO/MWCNT Films for Symmetric Supercapacitor Application. *Nanoscale Res. Lett.* **2019**, *14*, No. 266.
(57) Cougnon, C.; Lebègue, E.; Pognon, G. Impedance Spectroscopy Study of a Catechol-Modified Activated Carbon Electrode as Active Material in Electrochemical Capacitor. *J. Power Sources* **2015**, *274*, 551−559.

https://doi.org/10.1021/acsapm.2c01366
ACS Appl. Polym. Mater. XXXX, XXX, XXX−XXX

(58) Lee, H. U.; Jin, J.-H.; Kim, S. W. Effect of Gel Electrolytes on the Performance of a Minimized Flexible Micro-Supercapacitor Based on Graphene/PEDOT Composite Using Pen Lithography. *J. Ind. Eng. Chem.* **2019**, *71*, 184−190.
(59) Yan, D.; Li, Y.; Liu, Y.; Zhuo, R.; Geng, B.; Wu, Z.; Wang, J.; Ren, P.; Yan, P. Design and Influence of Mass Ratio on Supercapacitive Properties of Ternary Electrode Material Reduced Graphene Oxide@MnO_2@ Poly(3,4-ethylenedioxythiophene)-Poly-(styrene sulfonate). *Electrochim. Acta* **2015**, *169*, 317−325.
(60) Gonçalves, R.; Pereira, E. C.; Marchesi, L. F. The Over-oxidation of Poly(3-hexylthiophene) (P3HT) Thin Film: CV and EIS Measurements. *Int. J. Electrochem. Sci.* **2017**, 1983−1991.
(61) Sivaraman, P.; Bhattacharrya, A. R.; Mishra, S. P.; Thakur, A. P.; Shashidhara, K.; Samui, A. B. Asymmetric Supercapacitor Containing Poly(3-methyl thiophene)-Multiwalled Carbon Nanotubes Nanocomposites and Activated Carbon. *Electrochim. Acta* **2013**, *94*, 182−191.
(62) Lagoutte, S.; Aubert, P.-H.; Pinault, M.; Tran-Van, F.; Mayne-L'Hermite, M.; Chevrot, C. Poly(3-methylthiophene)/Vertically Aligned Multi-Walled Carbon Nanotubes: Electrochemical Synthesis, Characterizations and Electrochemical Storage Properties in Ionic Liquids. *Electrochim. Acta* **2014**, *130*, 754−765.
(63) He, H.; Zhang, L.; Guan, X.; Cheng, H.; Liu, X.; Yu, S.; Wei, J.; Ouyang, J. Biocompatible Conductive Polymers with High Conductivity and High Stretchability. *ACS Appl. Mater. Interfaces* **2019**, *11*, 26185−26193.
(64) Ega, S. P.; Srinivasan, P. Quinone Materials for Supercapacitor: Current Status, Approaches, and Future Directions. *J. Energy Storage* **2022**, *47*, No. 103700.
(65) Gouda, A.; Soavi, F.; Santato, C. Eumelanin Electrodes in Buffered Aqueous Media at Different pH Values. *Electrochim. Acta* **2020**, *347*, No. 136250.
(66) Sofen, S. R.; Cooper, S. R.; Raymond, K. N. Crystal and Molecular Structures of Tetrakis(Catecholato)Hafnate(IV) and -Cerate(IV). Further Evidence for a Ligand Field Effect in the Structure of Tetrakis(Catecholato)Uranate(IV). *Inorg. Chem.* **1979**, *18*, 1611−1616.
(67) Pham, T. A.; Altman, A. B.; Stieber, S. C. E.; Booth, C. H.; Kozimor, S. A.; Lukens, W. W.; Olive, D. T.; Tyliszczak, T.; Wang, J.; Minasian, S. G.; Raymond, K. N. A Macrocyclic Chelator That Selectively Binds Ln^{4+} over Ln^{3+} by a Factor of 10^{29}. *Inorg. Chem.* **2016**, *55*, 9989−10002.

https://doi.org/10.1021/acsapm.2c01366
ACS Appl. Polym. Mater. XXXX, XXX, XXX−XXX